chemosensors

MDPI

Article

AIPE-Active Fluorophenyl-Substituted Ir(III) Complexes for Detecting Trinitrophenols in Aqueous Media

Jiahao Du [1], Ruimin Chen [1], Xiaoran Yang [1], Xiaona Li [2,*] and Chun Liu [1,*]

[1] State Key Laboratory of Fine Chemicals, Frontier Science Center for Smart Materials, School of Chemical Engineering, Dalian University of Technology, Dalian 116024, China; dujiahao@mail.dlut.edu.cn (J.D.); chenruimin@mail.dlut.edu.cn (R.C.); yxiaoran@mail.dlut.edu.cn (X.Y.)

[2] Key Laboratory of Industrial Ecology and Environmental Engineering (MOE), School of Environmental Science and Technology, Dalian University of Technology, Dalian 116024, China

* Correspondence: klieee@dlut.edu.cn (X.L.); cliu@dlut.edu.cn (C.L.)

Abstract

Three fluorophenyl-substituted cyclometalated Ir(III) complexes (**Ir1**–**Ir3**) have been synthesized by changing the position of the fluorine atom. All complexes exhibit distinct aggregation-induced phosphorescence emission (AIPE) characteristics in CH_3CN/H_2O and demonstrate satisfactory detection performance for 2,4,6-trinitrophenols (TNPs) with limits of detection of 124 nM, 101 nM, and 127 nM, respectively. In addition, **Ir1**–**Ir3** possess excellent selectivity and anti-interference capability for TNP detection, showing outstanding performance even in different common water samples. The ultraviolet–visible absorption spectra and luminescence lifetimes of the complexes show that their quenching processes include both a static process and dynamic process, and the detection mechanism may be assigned to a combination of photo-induced electron transfer and an inner-filter effect.

Keywords: Ir(III) complexes; AIPE-active; 2,4,6-trinitrophenols; aqueous media

check for updates

Received: 8 July 2025
Revised: 12 August 2025
Accepted: 18 August 2025
Published: 20 August 2025

Citation: Du, J.; Chen, R.; Yang, X.; Li, X.; Liu, C. AIPE-Active Fluorophenyl-Substituted Ir(III) Complexes for Detecting Trinitrophenols in Aqueous Media. *Chemosensors* **2025**, *13*, 315. https://doi.org/10.3390/chemosensors13080315

Copyright: © 2025 by the authors. Licensee MDPI, Basel, Switzerland. This article is an open access article distributed under the terms and conditions of the Creative Commons Attribution (CC BY) license (https://creativecommons.org/licenses/by/4.0/).

1. Introduction

In 2001, Tang et al. proposed a new concept of aggregation-induced emission (AIE) [1]. In contrast to the aggregation-caused quenching (ACQ) phenomenon, the AIE phenomenon demonstrates that some molecules can significantly enhance their luminescence in aggregated states. The introduction of the AIE notion has broadened the range of applications for luminescent materials, and provides new direction for the development of luminescent materials [2–6]. In 2002, Mani et al. first discovered the phenomenon of aggregation-induced phosphorescence emission (AIPE) in transition metal complexes [7]. Compared to traditional luminescent molecules, transition metal complexes have the advantages of longer phosphorescence lifetime, higher quantum yield, and larger Stokes shift. Currently, studies on the AIPE properties of transition metal complexes have received a broad range of attention [8–10].

Ir(III) complexes possess excellent photothermal stability, adjustable luminescence characteristics, and high luminescence efficiency [11–15]. These make them valuable for applications in optoelectronic devices [16], biological imaging and therapy [17], and catalytic science [18]. In 2008, Zhao et al. reported AIPE-active Ir(III) complexes for the first time [19]. Subsequently, a series of AIPE-active Ir(III) complexes have been developed [20–22]. Recently, the use of Ir(III) complexes with AIPE properties as probes for monitoring environmental parameters, including organic pollutants [23], pH [24], and toxic gases [25], has received significant attention.

2,4,6-Trinitrophenol (TNP) is a type of nitro compound with powerful explosive properties and high sensitivity to temperature, friction, and impact. At the same time, it has a broad range of industrial applications, such as pharmaceuticals, leather processing, and raw materials for dyes and pigments [26,27]. However, it also pollutes the environment by entering the ecosystem through the medium of water, leading to soil and groundwater contamination [28,29]. Since TNP may persist in the environment, especially when TNP residues contaminate drinking water and agricultural land, it can directly affect human and animal health. Therefore, a highly sensitive, selective, and trace detection method for of TNP is urgently needed. Recently, the detection of TNP in aqueous media using Ir(III) complexes as sensors has attracted extensive interest [30–32]. However, the relationship between the molecular structures of the complexes and the detection performances, as well as the detection mechanism for TNP, still require further exploration.

In the past several years, our team has developed a series of Pt(II), Ir(III), and Ru(II) complexes for TNP detection [33–35]. We found that introducing a fluorophenyl group can significantly affect the AIPE properties and TNP detection performances of the corresponding Pt(II) complexes [35]. In this work, three fluorophenyl-substituted cyclometalated Ir(III) complexes, **Ir1**–**Ir3,** were synthesized and their properties were systematically studied in detail. The results indicate that **Ir1**–**Ir3** are all AIPE-active and demonstrate high selectivity and sensitivity for the detection of TNP in aqueous media, showing great potential as probes for TNP detection.

2. Materials and Methods

2.1. Materials and Instruments

Additional information for the instruments and materials used in this study can be seen in the Supporting Information.

2.2. Synthesis and Characterization of Complexes

Three fluorophenyl-substituted C^N ligands were synthesized according to the reported method (Figure S1) [36]. The Ir(III) complexes were synthesized by the following routes (Scheme 1): $IrCl_3 \cdot 3H_2O$ (0.2 mmol, 70.5 mg) and the C^N ligand (0.5 mmol, 124.5 mg) were added to a mixed solution of $EtOCH_2CH_2OH$ (9 mL) and H_2O (3 mL). The mixture was stirred for 24 h at 120 °C under N_2 to provide the dichlorobridge intermediate. Subsequently, the intermediate and 2,2′-bipyridine (0.6 mmol, 93.7 mg) were transferred into $EtOCH_2CH_2OH$ (12 mL) and the mixture was stirred for 24 h at 120 °C under N_2. At the end of the reaction, the reaction system was cooled to room temperature. An excess of saturated aqueous solution of KPF_6 (1.2 mmol, 220.9 mg) was added into the reaction system and the mixture was stirred at room temperature for 12 h. Finally, the target products of **Ir1**–**Ir3** were isolated and purified by column chromatography. The comprehensive characterizations for **Ir1**–**Ir3** are given in the Supporting Information (Figures S2–S13).

Ir1. An orange-yellow solid, 168.3 mg, yield: 85%. ^{1}H NMR (400 MHz, DMSO-d_6) δ 8.91 (d, J = 8.4 Hz, 2H), 8.31 (t, J = 7.7 Hz, 4H), 8.07–7.93 (m, 6H), 7.75 (t, J = 7.6 Hz, 2H), 7.70 (d, J = 5.9 Hz, 2H), 7.34–7.29 (m, 4H), 7.28–7.17 (m, 8H), 6.42 (d, J = 2.4 Hz, 2H).^{13}C NMR (151 MHz, DMSO-d_6) δ 166.25, 159.80, 158.16, 155.33, 150.06, 149.87, 148.97, 143.51, 139.64, 138.80, 136.31, 131.04, 131.01, 130.26, 130.24, 129.47, 129.42, 128.72, 128.00, 127.92, 125.04, 125.00, 124.76, 124.74, 124.03, 122.99, 120.28, 116.16, 116.01. ^{19}F NMR (470 MHz, DMSO-d_6) δ −69.39, −70.90, −117.53. HRMS (ESI, m/z): calcd for $C_{44}H_{30}N_4F_2Ir$ [M-PF_6]$^+$: 845.2068, found: 845.2061.

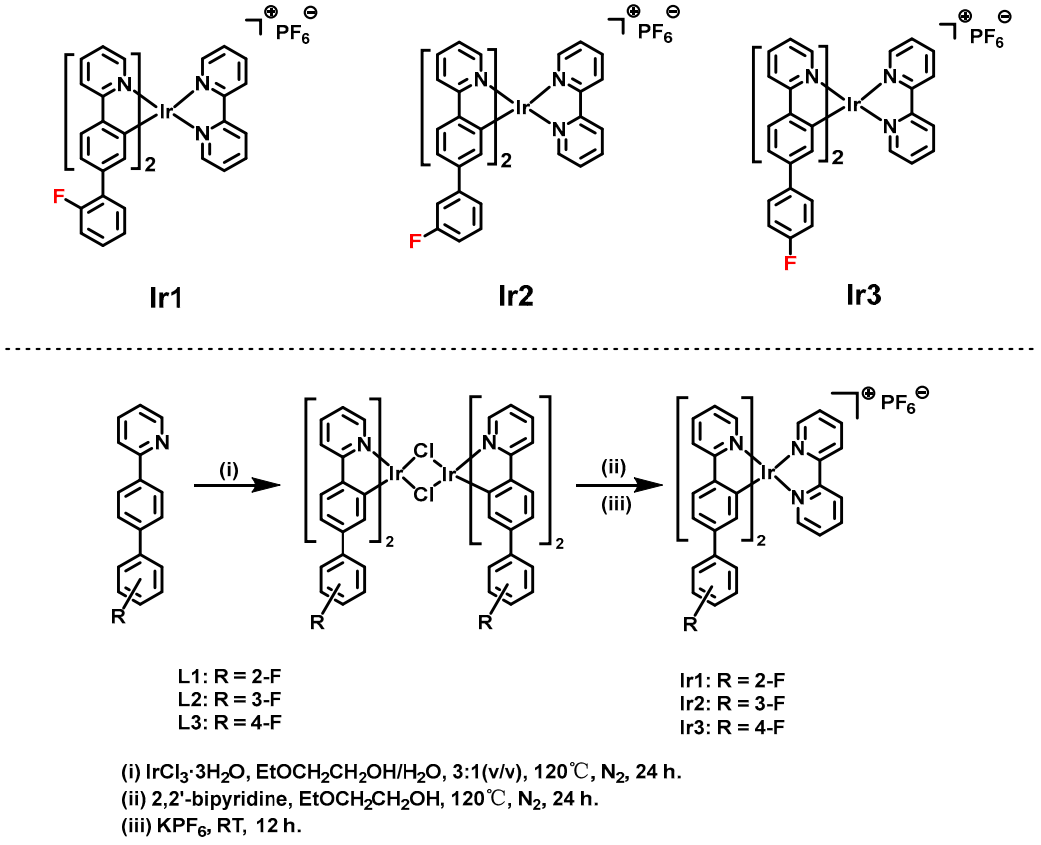

Scheme 1. Structures and the synthetic routes of **Ir1**–**Ir3**. (red markers indicate the different substitution positions of the F atoms).

Ir2. An orange-yellow solid, 182.2 mg, yield: 92%. ^{1}H NMR (400 MHz, DMSO-d_6) δ 8.91 (d, J = 8.3 Hz, 2H), 8.36 (d, J = 8.2 Hz, 2H), 8.29 (t, J = 7.9 Hz, 2H), 8.01 (dd, J = 11.6, 7.4 Hz, 6H), 7.74 (t, J = 5.3 Hz, 4H), 7.38 (td, J = 8.2, 4.0 Hz, 4H), 7.23 (t, J = 6.7 Hz, 2H), 7.18–7.08 (m, 6H), 6.41 (d, J = 2.0 Hz, 2H). ^{13}C NMR (151 MHz, DMSO-d_6) δ 166.20, 163.19, 161.58, 155.30, 150.83, 150.12, 149.18, 143.89, 142.55, 142.50, 139.86, 139.62, 138.83, 130.74, 130.69, 128.73, 128.58, 125.50, 124.96, 124.08, 122.34, 122.32, 121.33, 120.36, 114.25, 114.11, 113.01, 112.86. ^{19}F NMR (470 MHz, DMSO-d_6) δ −69.39, −70.90, −112.68. HRMS (ESI, m/z): calcd for $C_{44}H_{30}N_4F_2Ir$ [M-PF_6]$^+$: 845.2068, found: 845.2065.

Ir3. An orange-yellow solid, 178.2 mg, yield: 90%. ^{1}H NMR (400 MHz, DMSO-d_6) δ 8.91 (d, J = 8.3 Hz, 2H), 8.30 (q, J = 8.0 Hz 4H), 7.99 (q, J = 8.0 Hz, 6H), 7.72 (t, J = 6.6 Hz, 4H), 7.37–7.31 (m, 6H), 7.21 (t, J = 8.1 Hz, 6H), 6.39 (s, 2H). ^{13}C NMR (151 MHz, DMSO-d_6) δ 165.80, 162.10, 160.48, 154.80, 150.41, 149.54, 148.55, 142.73, 139.82, 139.11, 138.29, 136.01, 136.00, 128.22, 128.05, 127.77, 127.72, 124.99, 124.45, 123.41, 120.64, 119.71, 115.18, 115.04. ^{19}F NMR (470 MHz, DMSO-d_6) δ −69.39, −70.90, −115.05. HRMS (ESI, m/z): calcd for $C_{44}H_{30}N_4F_2Ir$ [M-PF_6]$^+$: 845.2068, found: 845.2064.

2.3. Tests for the Detection of TNP

Stock solutions of each of **Ir1**–**Ir3** (c = 100 μM) were prepared in CH_3CN. Then, eight 3 mL suspensions were prepared by taking the stock solution (v = 300 μL) and adding different volumes of CH_3CN and H_2O. In this way, suspensions with different water contents (0–90%, c = 10 μM) were prepared. For each suspension, 3 mL of them was placed into quartz cuvettes, and then the emission spectra were recorded to study the properties of **Ir1**–**Ir3**.

The suspensions of **Ir1**–**Ir3** (**Ir1**: f_w = 60%, **Ir2**: f_w = 70%, **Ir3**: f_w = 70%, in CH_3CN/H_2O) were prepared in volumetric flasks (200 mL). Then, 11 blank suspension

samples of **Ir1**–**Ir3** were randomly selected, and their emission spectra were measured after equilibrium. TNP solutions, with concentrations varying from 0.1 to 20 mM, were prepared in CH_3CN/H_2O. The TNP solutions (30 μL) at different concentrations were added to the **Ir1**–**Ir3** suspensions (3 mL), and the emission spectra were recorded after allowing the system to equilibrate. In the experiments on selectivity and competition for the detection of TNP, seven analytes with structures partially similar to TNP were selected for testing. The analytes included: 4-Methoxyphenol (MEHQ), 2-Nitrotoluene (2-NT), Nitromethane (NM-55), Phenol, 2-Cresol, 3-Cresol, and 4-Cresol. During the testing process, 30 μL (c = 20 mM) of the analytes was added to each of the **Ir1**–**Ir3** suspensions. To further investigate the anti-interference capability of **Ir1**–**Ir3**, 30 μL (c = 20 mM) of eight common ionic compounds was added to each complex suspension. The ionic compounds included the following: KF, KBr, NaOAc, $ZnCl_2$, $CaCl_2$, $NiCl_2$, $CuSO_4$, and $CoCO_3$. Finally, lake water, rainwater, seawater, and tap water were selected for testing in place of deionized water to assess the universality of the complexes in different common water samples. The lake water was collected from Lingshui Lake at Dalian University of Technology, the seawater was collected from Qixianling, Dalian, and the tap water was collected from Dalian University of Technology.

Be cautious! Nitroaromatic compounds are explosive and should be processed in small amounts in a well-ventilated environment. Avoid exposure to high temperatures, open flames, and impact. Always wear appropriate protective equipment.

3. Results and Discussion

3.1. Photophysical Properties

The photophysical properties of **Ir1**–**Ir3** were tested by UV–vis absorption and emission spectrometers. The UV–vis absorption spectra of **Ir1**–**Ir3** exhibit strong absorption bands at 220–320 nm (Figure 1a), which is probably related to the π-π* transitions in the ligand center. Additionally, weak absorption features are observed at wavelengths of 380–450 nm, likely originating from metal-to-ligand charge transfer (MLCT) and ligand–ligand charge transfer (LLCT) [37]. Figure 1b shows the normalized emission spectra of **Ir1**–**Ir3** in CH_3CN, and their maximum emission wavelengths are 574 nm, 573 nm, and 578 nm, respectively. More data about the photophysical properties of **Ir1**–**Ir3** can be found in Table S1 of the Supporting Information.

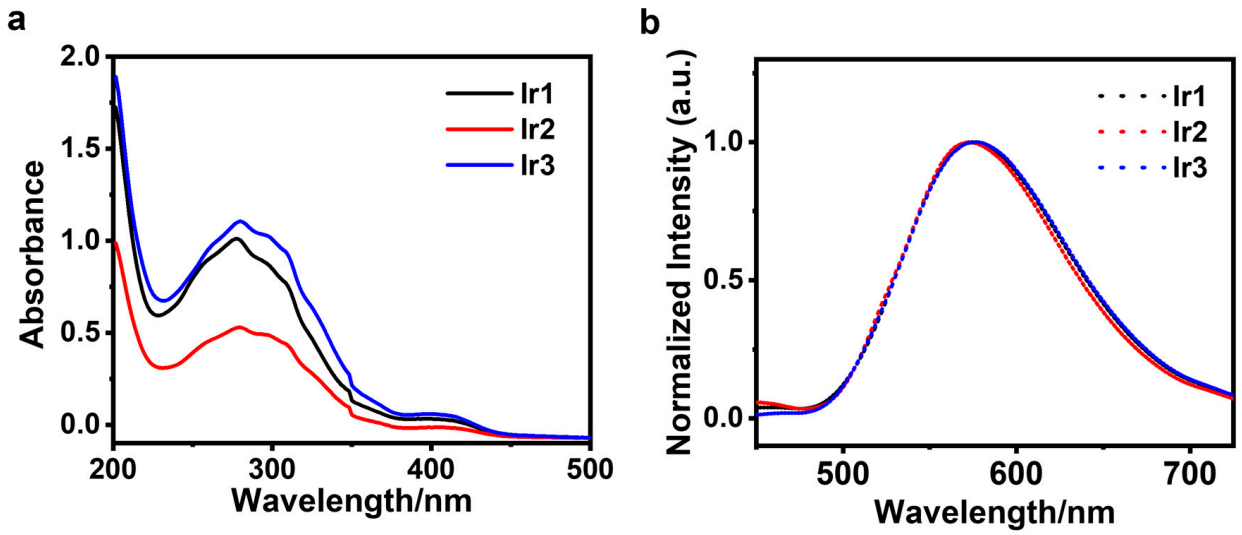

Figure 1. (**a**) The UV–vis absorption spectra and (**b**) the normalized emission spectra of **Ir1**–**Ir3** in CH_3CN (excitation wavelength: 400 nm, c = 10 μM).

3.2. AIPE Properties and Stability Testing

The luminescence properties of **Ir1**–**Ir3** were initially tested by recording their emission spectra in CH_3CN/H_2O with different water contents. As shown in Figure 2, there is a significant enhancement of the emission intensities with an increase in water content from 0% to 70%. We speculate that the addition of water, as a poor solvent, causes the aggregation of the complex molecules, thus they exhibit good AIPE properties. Subsequently, dynamic light scattering (DLS) experiments were performed to verify whether **Ir1**–**Ir3** had undergone aggregation (Figure S14 in Supporting Information). It can be seen that **Ir1**–**Ir3** indeed produce aggregates at the selected water contents (**Ir1**: f_w = 60%, **Ir2**: f_w = 70%, **Ir3**: f_w = 70%), and their hydrodynamic diameters are 20.96 nm, 57.36 nm, and 51.33 nm, respectively. The above results confirm that **Ir1**–**Ir3** exhibit significant AIPE properties.

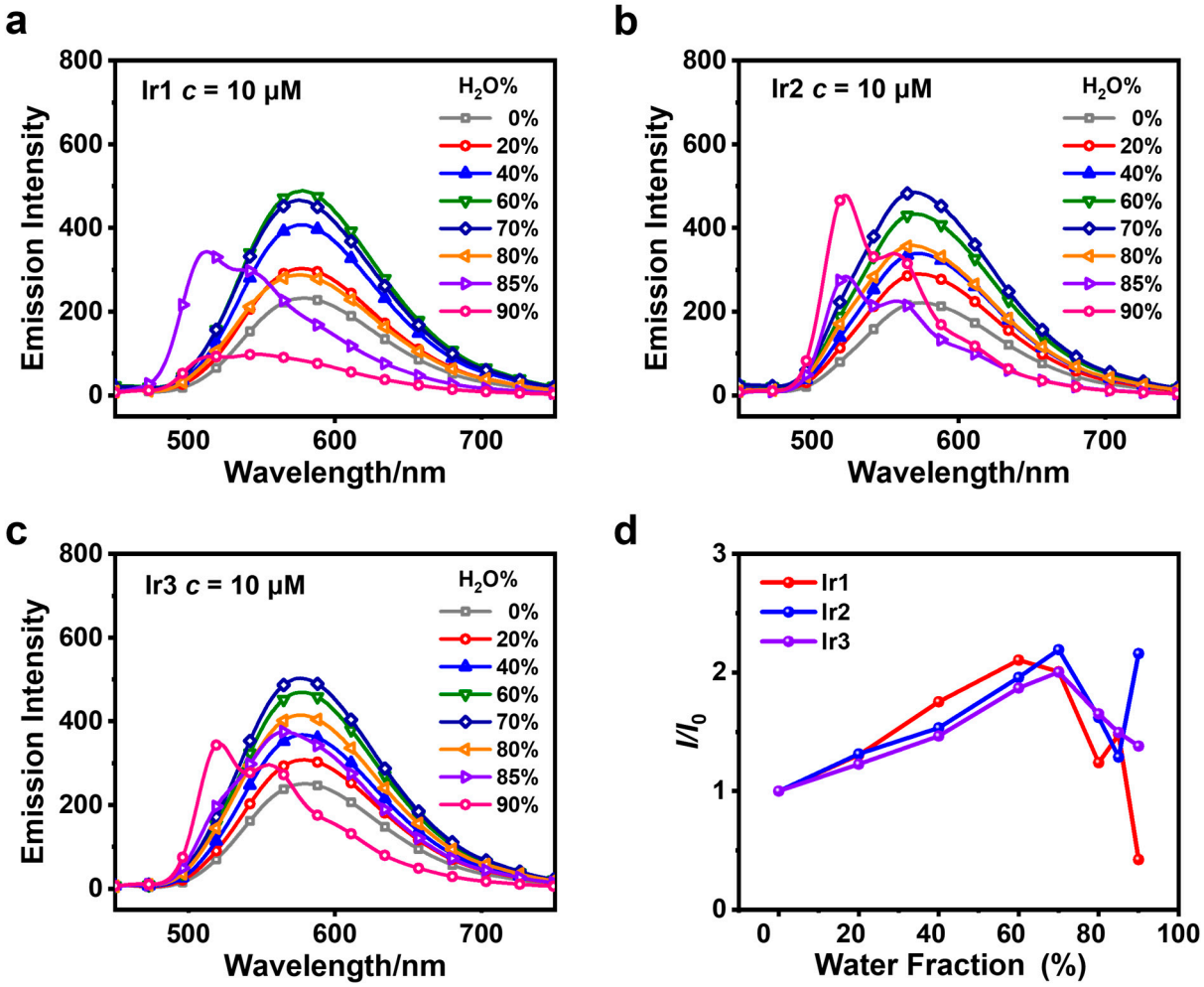

Figure 2. The emission spectra of (**a**) **Ir1**, (**b**) **Ir2**, and (**c**) **Ir3** in CH_3CN/H_2O mixtures with varying water contents and (**d**) the relative intensities I/I_0 of **Ir1**–**Ir3**. I represents the emission intensities at the maximum emission wavelength in different water contents (**Ir1**: 574 nm; **Ir2**: 573 nm; **Ir3**: 578 nm), while I_0 represents the emission intensities at the maximum emission wavelength in CH_3CN (excitation wavelength: 400 nm, c = 10 μM).

Then, the stabilities of **Ir1**–**Ir3** were analyzed by their emission spectra. The results show that **Ir1**–**Ir3** reach equilibrium after 8 h, 7 h, and 4 h, respectively (Figure 3). Then, the emission spectra of 11 blank suspensions of the complexes were tested after equilibrium to calculate the standard deviations (Table 1).

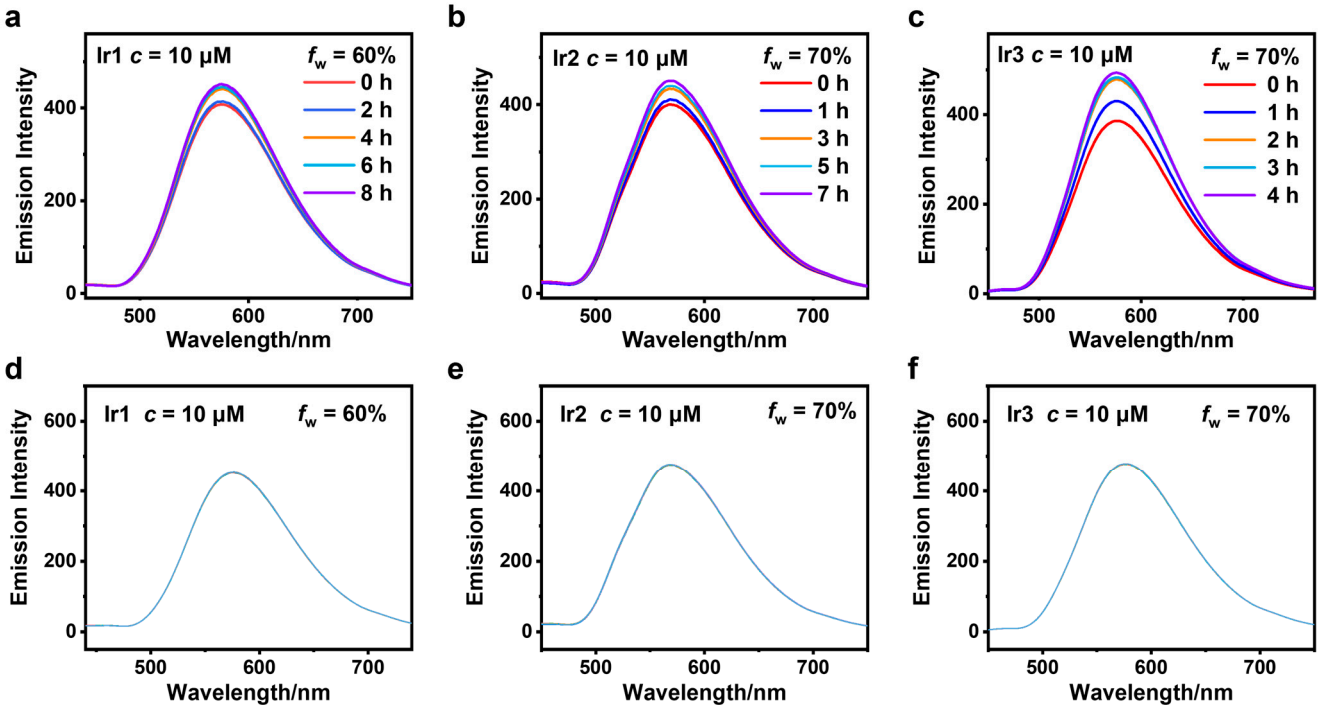

Figure 3. The emission spectra of (**a**) **Ir1** (f_w = 60%), (**b**) **Ir2** (f_w = 70%), and (**c**) **Ir3** (f_w = 70%) in volumetric flasks after being left for different durations, as well as the emission spectra of 11 blank suspension samples for (**d**) **Ir1**, (**e**) **Ir2**, and (**f**) **Ir3** after reaching equilibrium at 8 h, 7 h, and 4 h, respectively (excitation wavelength: 400 nm, c = 10 μM).

Table 1. The standard deviations and emission intensities of **Ir1**–**Ir3** at 574 nm, 573 nm, and 578 nm, respectively (**Ir1**: f_w = 60%, **Ir2**: f_w = 70%, **Ir3**: f_w = 70%; excitation wavelength: 400 nm, c = 10 μM).

Complex	Ir1	Ir2	Ir3
λ/nm	574	573	578
X_1	452.1	473.1	477.0
X_2	452.4	473.5	476.6
X_3	452.4	474.6	476.7
X_4	451.9	473.6	476.4
X_5	451.2	474.4	476.8
X_6	451.4	473.9	476.7
X_7	451.3	473.4	477.0
X_8	451.2	473.2	477.6
X_9	452.1	473.9	477.5
X_{10}	451.9	474.0	477.4
X_{11}	452.3	473.5	477.8
σ	0.4558	0.4518	0.4400

X_i (i = 1, 2, 3...., 11) stands for the emission intensity of each sample, i stands for the number of the sample, and σ is the standard deviation.

3.3. Sensing of TNP

Ir1–**Ir3** exhibit significant AIPE properties, which indicates their potential to act as probes for detecting TNP. Therefore, we prepared suspensions of **Ir1**–**Ir3** in CH_3CN/H_2O (**Ir1**: f_w = 60%, **Ir2**: f_w = 70%, **Ir3**: f_w = 70%), and performed TNP titration tests after reaching equilibrium (illustrated in Figure 4). The results show that as the concentration of TNP increases, the emission intensities of **Ir1**–**Ir3** significantly decrease. The quenching efficiencies of **Ir1**–**Ir3** are 18%, 22%, and 17%, respectively, at a TNP concentration of 8 μM (0.8 equiv.). When the TNP concentration increases to 200 μM (20.0 equiv.), the quenching efficiencies of **Ir1**–**Ir3** all exceed 95%. To calculate the quenching constants

(K_{SV}) for the detection of TNP, the ratios of the emission intensities before the addition of TNP (I_0) to the emission intensities after the addition of TNP (I) were plotted (Figure 4). The Stern–Volmer curves for **Ir1**–**Ir3** are overall non-linear. But at low concentrations of TNP (0–8 μM), the I_0/I ratios of **Ir1**–**Ir3** exhibit a clear linear relationship, indicating that it is a static quenching process. The Stern–Volmer plots show a non-linear relationship with increasing concentrations of TNP. This indicates that the luminescence quenching process involves both static and dynamic quenching [38]. According to the Stern–Volmer equation ($I_0/I = K_{SV}[Q] + 1$), the quenching constants for **Ir1**–**Ir3** were obtained in the low concentration range through fitting, with values of 2.7×10^4 M^{-1}, 3.3×10^4 M^{-1}, and 2.3×10^4 M^{-1}, respectively.

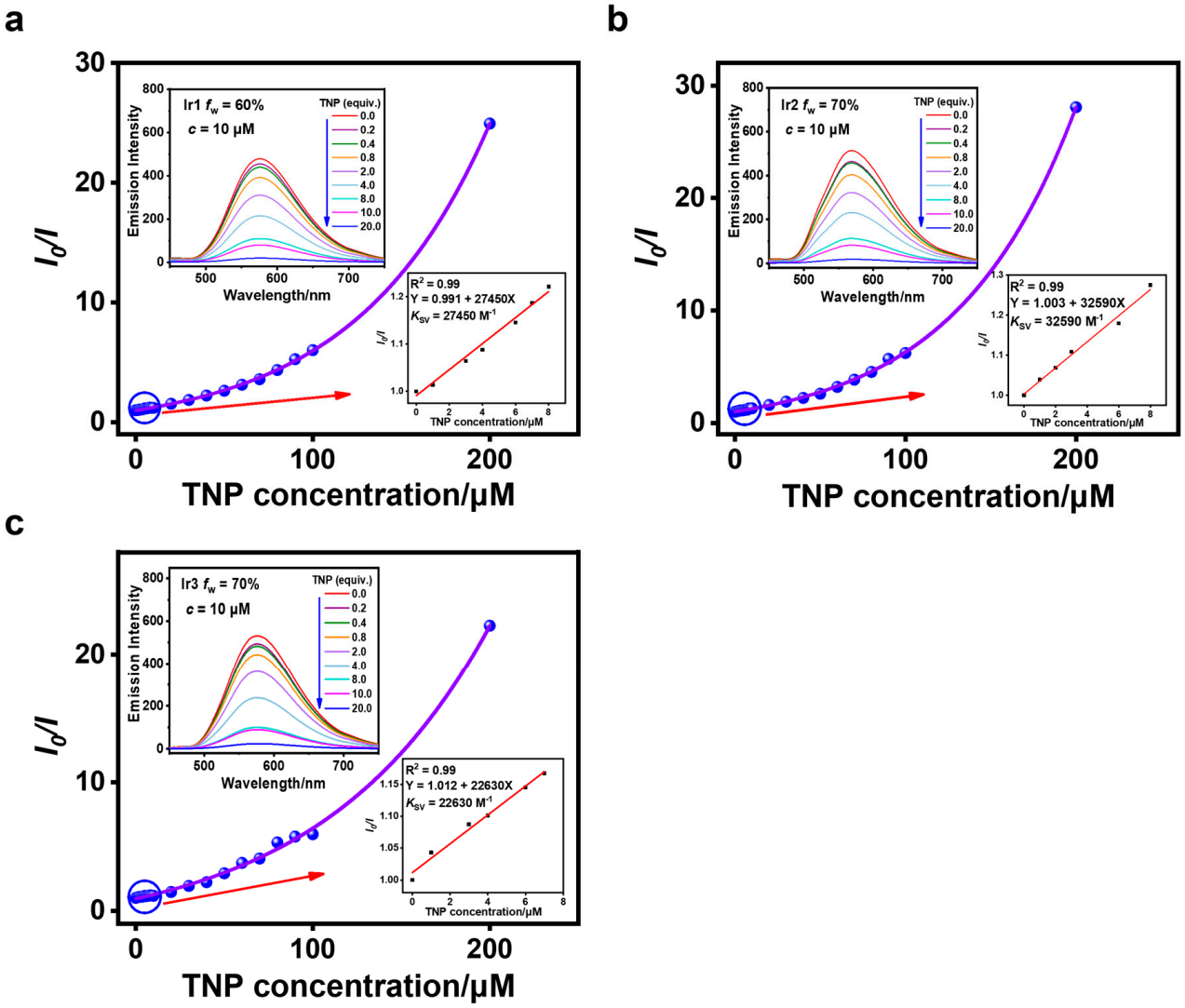

Figure 4. The Stern–Volmer curves of (**a**) **Ir1** (f_w = 60%), (**b**) **Ir2** (f_w = 70%), and (**c**) **Ir3** (f_w = 70%) for the detection of TNP. Inset: The emission spectra of the complexes in the presence of TNP at different concentrations (top left) and the linear portion of the Stern–Volmer curve (bottom right).

Within the low concentration range (0–8 μM), linear regression analyses are performed on the emission intensities of **Ir1**–**Ir3** to calculate their slopes K (Figure 5). The limits of detection (LODs) for **Ir1**–**Ir3** are calculated according to the formula $LOD = 3\sigma/|K|$, with values of 124 nM, 101 nM, and 127 nM, respectively. Compared to the previously reported complexes [39–41], **Ir1**–**Ir3** exhibit extremely low LODs, demonstrating excellent performance for the detection of TNP (Table S2 in Supporting Information).

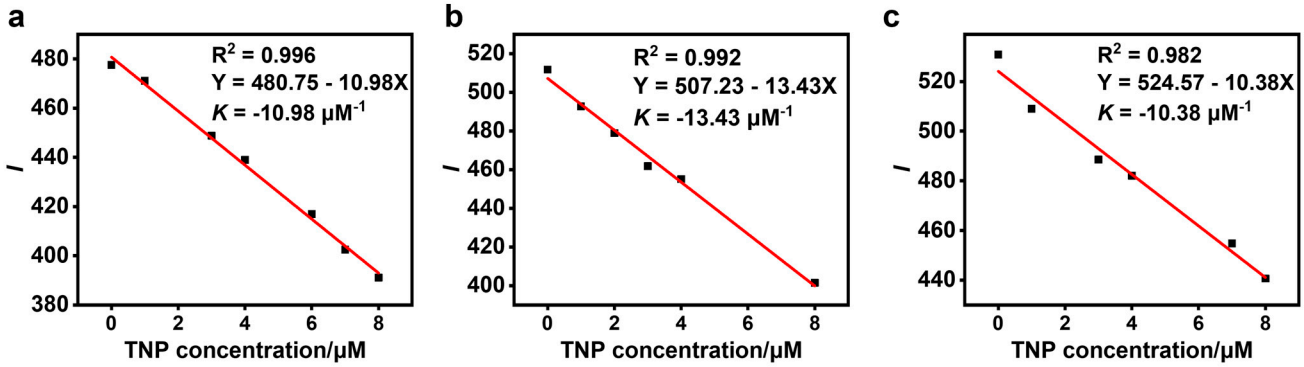

Figure 5. The emission intensity versus TNP concentration relationships for (**a**) **Ir1** (f_w = 60%), (**b**) **Ir2** (f_w = 70%), and (**c**) **Ir3** (f_w = 70%) (excitation wavelength: 400 nm, c = 10 μM).

3.4. Selectivity and Anti-Interference Capability Experiments

First, selective and competitive experiments were performed on **Ir1**–**Ir3**. Seven analytes (MEHQ, 2-NT, NM-55, Phenol, 2-Cresol, 3-Cresol, and 4-Cresol) were individually added to **Ir1**–**Ir3** suspensions. The emission spectra before and after the addition of TNP were tested. The results show that the addition of these analytes has little effect on the luminescence of the complex samples (<6% for all analytes except 2-NT, which is approximately 20%), and there are small changes in emission intensities (Figure 6). The luminescence quenching rates of all samples exceed 94% after the addition of TNP. In summary, the effects of other analytes on the emission intensities of the samples are much smaller than those of TNP, and **Ir1**–**Ir3** show excellent selectivity for TNP.

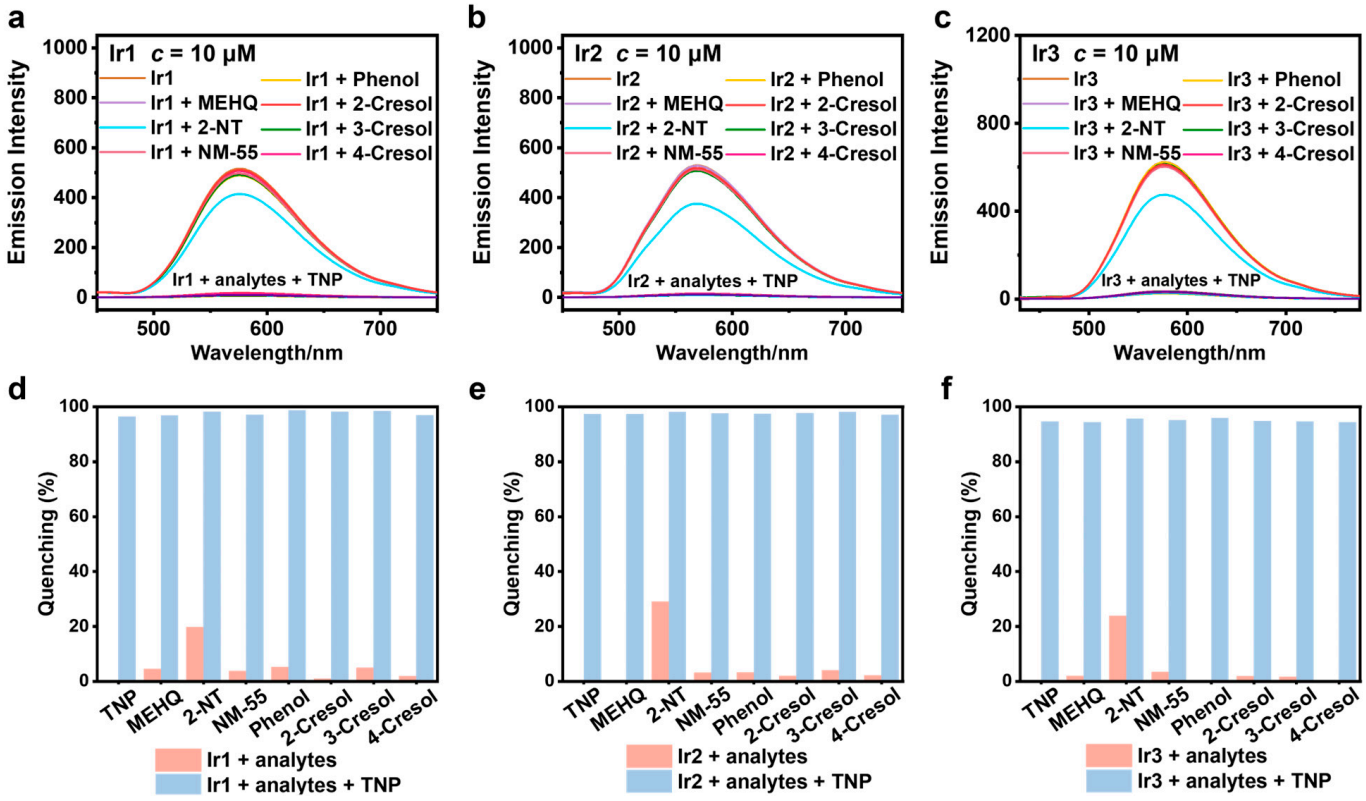

Figure 6. The emission spectra of (**a**) **Ir1** (f_w = 60%), (**b**) **Ir2** (f_w = 70%), and (**c**) **Ir3** (f_w = 70%) after the addition of different analytes (20 equiv.) and the quenching rates of different analytes on (**d**) **Ir1**, (**e**) **Ir2**, and (**f**) **Ir3** (excitation wavelength: 400 nm, c = 10 μM, CH_3CN/H_2O).

Next, an in-depth study was conducted on the anti-interference capability of **Ir1**–**Ir3**. Eight common ionic compounds (KF, KBr, NaOAc, $ZnCl_2$, $CaCl_2$, $NiCl_2$, $CuSO_4$, and $CoCO_3$) were individually added to **Ir1**–**Ir3** suspensions, and the emission spectra before and after the addition of TNP were tested as well. The results show that the addition of common ionic compounds has a negligible effect on the emission intensities and a minimal effect on the quenching efficiencies of **Ir1**–**Ir3** (<7% for all compounds; Figure 7). Furthermore, the luminescence quenching effects of the samples are not affected by these ionic compounds after the addition of TNP, and the luminescence quenching rates reach over 94% in all cases. These experimental results indicate that **Ir1**–**Ir3** show outstanding anti-interference capability when used for the detection of TNP. They effectively avoid effects from common ionic compounds, ensuring the accuracy and reliability of the detection results.

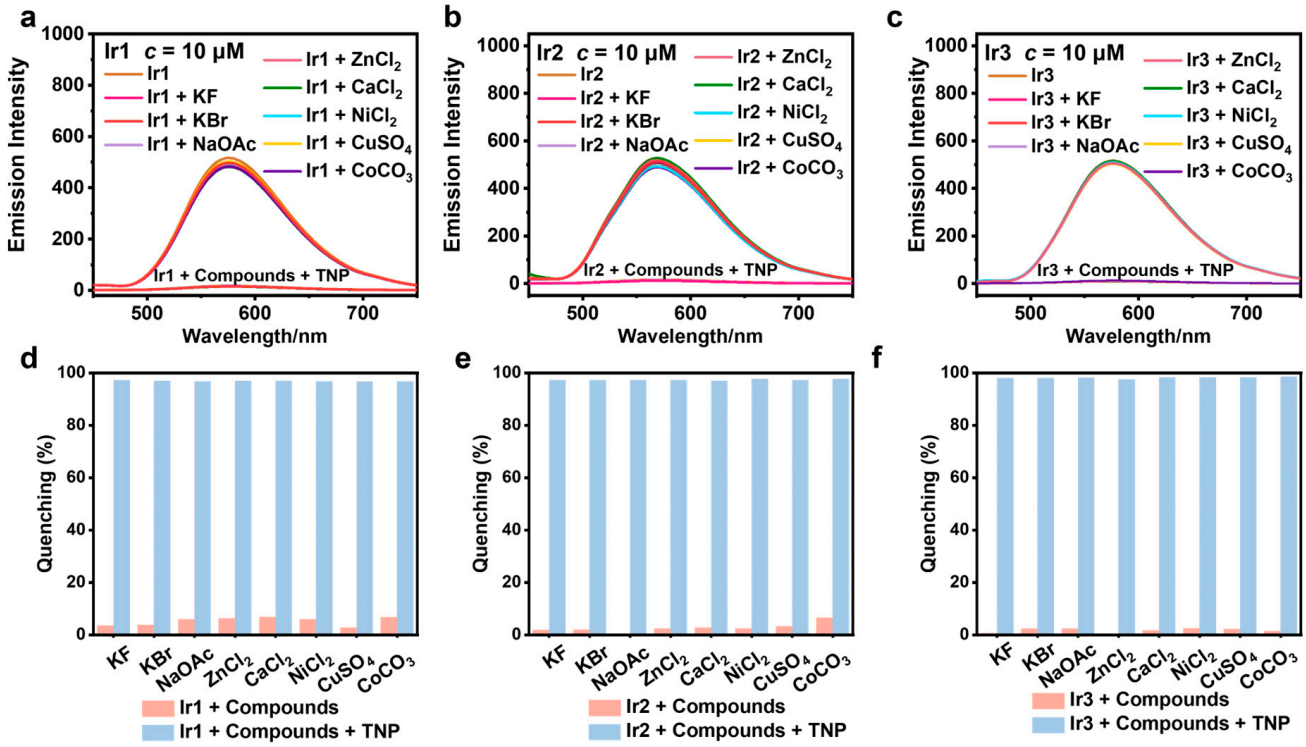

Figure 7. The emission spectra of (**a**) **Ir1** (f_w = 60%), (**b**) **Ir2** (f_w = 70%), and (**c**) **Ir3** (f_w = 70%) after the addition of different ionic compounds (20 equiv.) and the quenching rates of different ionic compounds on (**d**) **Ir1**, (**e**) **Ir2**, and (**f**) **Ir3** (Excitation wavelength: 400 nm, c = 10 μM, CH_3CN/H_2O).

Finally, the emission spectra of **Ir1**–**Ir3** were tested using lake water, rainwater, seawater, or tap water in place of deionized water. This was to assess the universality of **Ir1**–**Ir3** for the detection of TNP. The results show that the emission intensities of **Ir1**–**Ir3** are not affected by different water samples after the addition of TNP, and they still show excellent selectivity for TNP (Figure 8). The quenching effects in different water samples are similar to those in deionized water, and the quenching rates still reach over 94%. This indicates that despite the differences in water quality, **Ir1**–**Ir3** not only exhibit remarkable stability and efficiency but also demonstrate an excellent ability to detect TNP in different environments, showing great potential for applications.

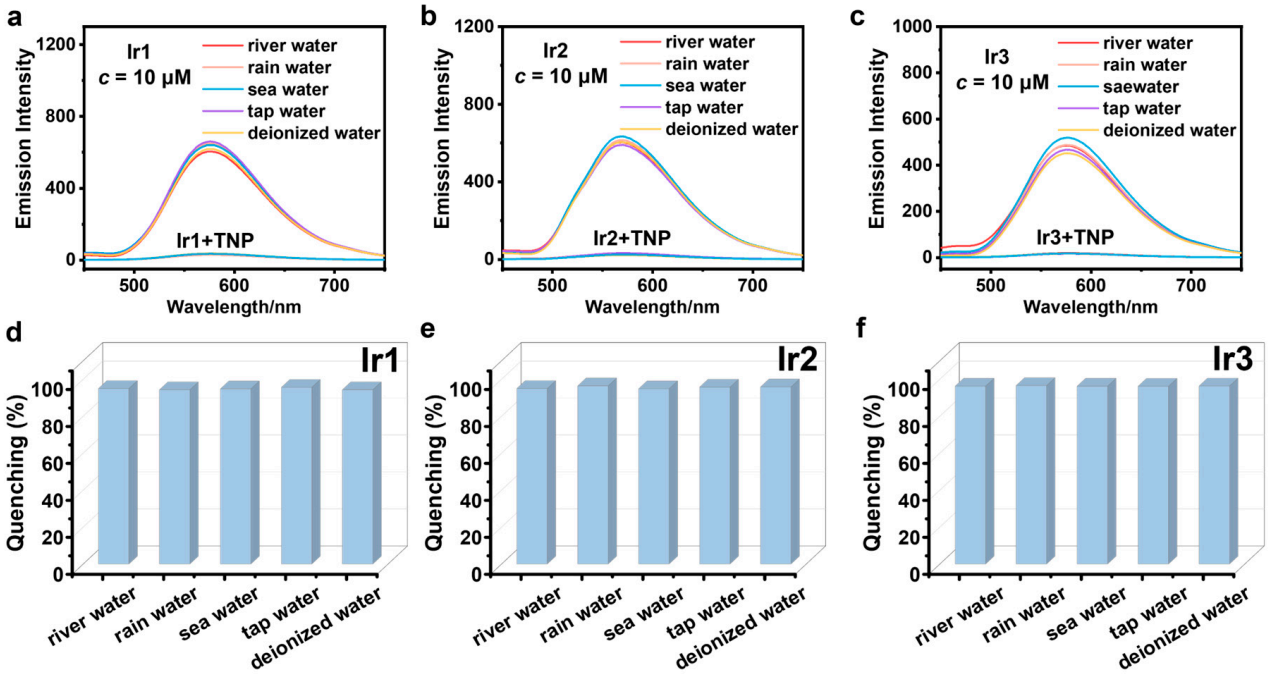

Figure 8. The emission spectra of (**a**) **Ir1** (f_w = 60%), (**b**) **Ir2** (f_w = 70%), and (**c**) **Ir3** (f_w = 70%) in different water samples and the quenching rates of (**d**) **Ir1**, (**e**) **Ir2**, and (**f**) **Ir3** in different water samples (excitation wavelength: 400 nm, c = 10 μM, CH_3CN/H_2O).

3.5. Sensing Mechanism

There are two common types of luminescence quenching process: one is static quenching and the other is dynamic quenching [42]. Static quenching refers to the interaction between the luminescent molecules and the quenchers, forming non-luminescent ground-state complexes [43]. These complexes inhibit the luminescence of the luminophores, leading to a decrease in their intensities. Dynamic quenching refers to the process in collisions between the luminophores and the quenchers, which lead to energy or a charge transfer [44]. Dynamic quenching is usually a rapid process and its rate is influenced by the concentration of quenchers and the collision frequency between molecules. At the same time, this process is accompanied by the decay of the luminescence lifetime [45].

To study the quenching processes of **Ir1**–**Ir3**, UV–vis absorption spectra were recorded (Figure 9a). As the concentrations of TNP increase, the absorption peak at 257 nm of **Ir1** exhibits a slight shift, and the absorption peak at 278 nm disappears, while **Ir2** and **Ir3** show similar behaviors (Figures S15a and S16a in Supporting Information). This suggests that static quenching may be involved in the quenching process. To confirm whether dynamic quenching is also present in the quenching process, we further conducted luminescence lifetime measurements (Figure 9b, Figures S15b and S16b in Supporting Information). At a low concentration range (TNP concentrations from 0 to 10 μM), the luminescence lifetimes of the complexes remain essentially unchanged. While in the high concentration range, the luminescence lifetimes of the complexes decrease significantly (Figure S17 in Supporting Information). This suggests that the quenching process for the detection of TNP by **Ir1**–**Ir3** may involve both static quenching and dynamic quenching.

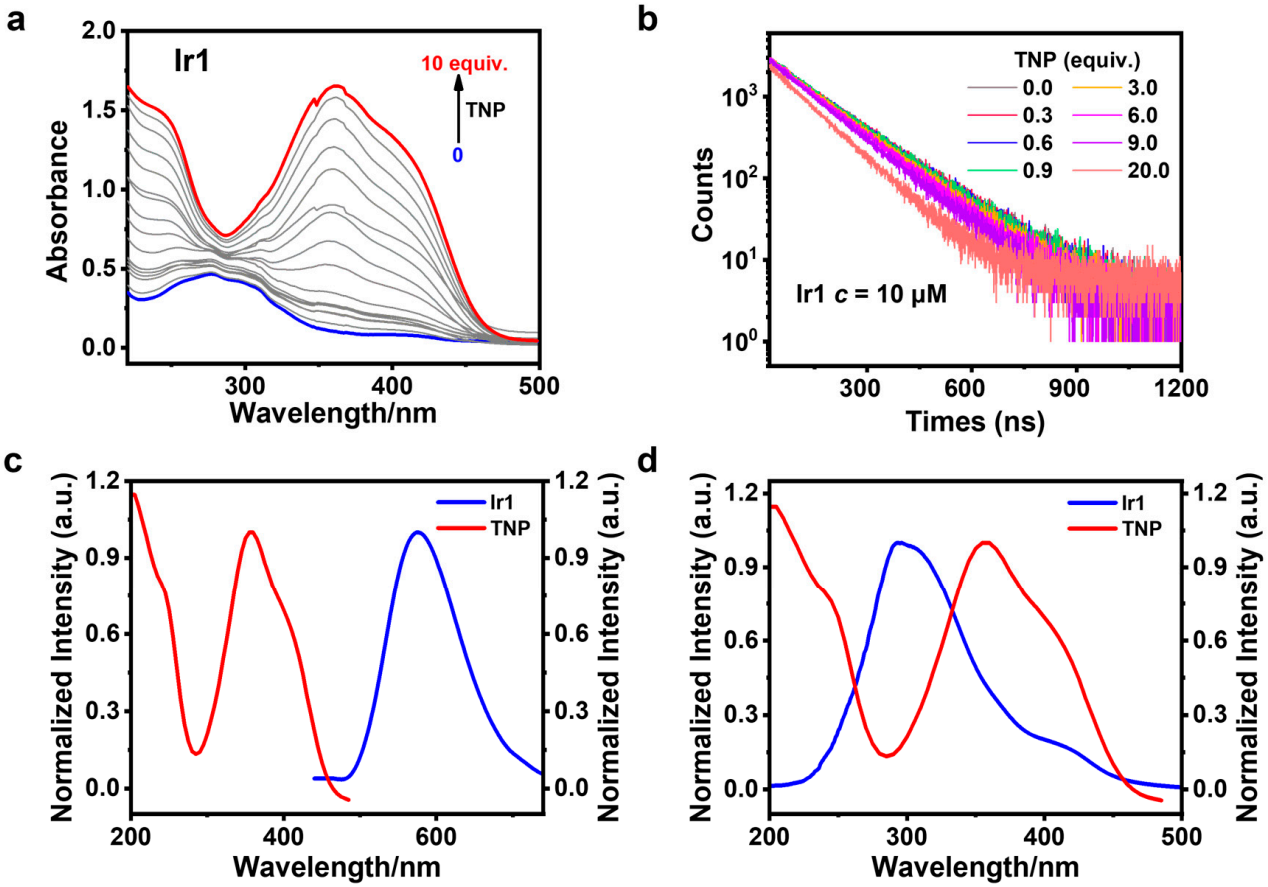

Figure 9. (**a**) The UV–vis absorption spectra of **Ir1** upon the addition of TNP with different concentrations; (**b**) the changes in luminescence lifetime of **Ir1** upon the addition of TNP with different concentrations; (**c**) the normalized UV–vis absorption spectrum of TNP (red line) and the normalized emission spectrum of **Ir1** (blue line); (**d**) the normalized UV–vis absorption spectrum of TNP (red line) and the normalized excitation spectrum of **Ir1** (blue line).

The common TNP detection mechanisms include Förster resonance energy transfer (FRET), photo-induced electron transfer (PET), and the inner-filter effect (IFE) [46]. By plotting the emission spectra of **Ir1**–**Ir3** and UV–vis absorption spectrum of TNP, it can be seen that these two spectra do not overlap (Figure 9c, and Figures S15c and S16c in Supporting Information), which rules out the FRET mechanism. We performed density functional theory calculations on **Ir2**, which has the lowest detection limit, and the results show that the PET mechanism is present in the detection process (Figure S18 in Supporting Information). In addition, the excitation spectra of **Ir1**–**Ir3** and the UV–vis absorption spectrum of TNP were also plotted (Figure 9d, and Figures S15d and S16d in Supporting Information). The excitation spectra of **Ir1**–**Ir3** show partial overlap with the absorption spectrum of TNP, suggesting that there may be IFE in the detection process. In addition, the quenching rates of **Ir1**–**Ir3** were tested at different excitation wavelengths to determine the effect of IFE on quenching (Figure S19 in Supporting Information). The results show that during the quenching process, the influence of IFE on the quenching is much smaller than that of PET [47]. Therefore, it can be deduced that the detection mechanism may be the result of the combined effects of PET and IFE. At the same time, the ^{1}H NMR spectra of **Ir1**–**Ir3** and TNP before and after mixing were tested and demonstrated that the addition of TNP does not lead to decomposition of **Ir1**–**Ir3** (Figures S20–S22 in Supporting Information).

4. Conclusions

In this work, three fluorophenyl-substituted cyclometalated Ir(III) complexes have been synthesized by altering the position of the fluorine atom. The results show that all the complexes possess obvious AIPE properties and exhibit high stability, high selectivity, and excellent anti-interference capability for TNP detection in aqueous media. The K_{SV} for **Ir1**–**Ir3** are 2.7×10^4 M^{-1}, 3.3×10^4 M^{-1}, and 2.3×10^4 M^{-1}, respectively. Their LODs are 124 nM, 101 nM, and 127 nM, respectively. **Ir2**, with a fluorine atom at the *meta* position, has the highest K_{SV} and the lowest LOD. Their quenching processes include both a dynamic quenching process and static quenching process, and the quenching mechanism may be attributed to the combination of PET and IFE. This study has enriched the development and application of Ir(III) complexes as luminescent probes for the detection of TNP.

Supplementary Materials: The following supporting information can be downloaded at: https://www.mdpi.com/article/10.3390/chemosensors13080315/s1, Figure S1: Synthesis routes of ligands **L1**–**L3**. Figure S2: The ^{1}H NMR spectrum of **Ir1** in DMSO-d_6. Figure S3: The high-resolution mass spectrum of **Ir1**. Figure S4: The ^{13}C NMR spectrum of **Ir1** in DMSO-d_6. Figure S5: The ^{19}F NMR spectrum of **Ir1** in DMSO-d_6. Figure S6: The ^{1}H NMR spectrum of **Ir2** in DMSO-d_6. Figure S7: The high-resolution mass spectrum of **Ir2**. Figure S8: The ^{13}C NMR spectrum of **Ir2** in DMSO-d_6. Figure S9: The ^{19}F NMR spectrum of **Ir2** in DMSO-d_6. Figure S10: The ^{1}H NMR spectrum of **Ir3** in DMSO-d_6. Figure S11: The high-resolution mass spectrum of **Ir3**. Figure S12: The ^{13}C NMR spectrum of **Ir3** in DMSO-d_6. Figure S13: The ^{19}F NMR spectrum of **Ir3** in DMSO-d_6. Table S1: Photophysical properties of **Ir1**–**Ir3**. Figure S14: DLS analysis of (a) **Ir1**, (b) **Ir2,** and (c) **Ir3** in CH_3CN/H_2O mixtures (**Ir1**: f_w = 60%, **Ir2**: f_w = 70%, **Ir3**: f_w = 70%). Table S2: Some reported complexes for the detection of TNP. Figure S15: (a) The UV–vis absorption spectra of **Ir2** upon the addition of TNP with different concentrations; (b) The changes in luminescence lifetime of **Ir2** upon the addition of TNP with different concentrations; (c) The normalized UV–vis absorption spectrum of TNP (red line) and the normalized emission spectrum of **Ir2** (blue line); (d) The normalized UV–vis absorption spectrum of TNP (red line) and the normalized excitation spectrum of **Ir2** (blue line). Figure S16: (a) The UV–vis absorption spectra of **Ir3** upon the addition of TNP with different concentrations; (b) The changes in luminescence lifetime of **Ir3** upon the addition of TNP with different concentrations; (c) The normalized UV–vis absorption spectrum of TNP (red line) and the normalized emission spectrum of **Ir3** (blue line); (d) The normalized UV–vis absorption spectrum of TNP (red line) and the normalized excitation spectrum of **Ir3** (blue line). Figure S17: Lifetimes of (a) **Ir1** (f_w = 60%), (b) **Ir2** (f_w = 70%), and (c) **Ir3** (f_w = 70%) in CH_3CN/H_2O after the addition of TNP with different concentrations. Insert: Lifetimes in the low concentration range (0–10 μM). Figure S18: Energy level diagrams of **Ir2** and TNP obtained from theoretical calculations. Figure S19: The quenching rates of (a) **Ir1** (f_w = 60%), (b) **Ir2** (f_w = 70%), and (c) **Ir3** (f_w = 70%) at different excitation wavelengths (310–440 nm). Figure S20: The ^{1}H NMR spectra of **Ir1**, TNP, and **Ir1** + TNP in DMSO-d_6. Figure S21: The ^{1}H NMR spectra of **Ir2**, TNP, and **Ir2** + TNP in DMSO-d_6. Figure S22: The ^{1}H NMR spectra of **Ir3**, TNP, and **Ir3** + TNP in DMSO-d_6.

Author Contributions: Investigation, J.D., R.C., and X.Y.; data curation, visualization, writing—original draft, J.D., R.C., and C.L.; writing—review and editing, X.Y., X.L., and C.L.; funding acquisition, supervision, C.L. All authors have read and agreed to the published version of the manuscript.

Funding: The authors thank the financial support from the National Natural Science Foundation of China (21978042) and the Fundamental Research Funds for the Central Universities (DUT22LAB610).

Institutional Review Board Statement: Not applicable.

Informed Consent Statement: Not applicable.

Data Availability Statement: Data are contained within the article.

Conflicts of Interest: The authors declare no conflicts of interest.

References

1. Luo, J.D.; Xie, Z.L.; Lam, J.W.Y.; Cheng, L.; Chen, H.Y.; Qiu, C.F.; Kwok, H.S.; Zhan, X.W.; Liu, Y.Q.; Zhu, D.B. Aggregation-induced emission of 1-methyl-1,2,3,4,5-pentaphenylsilole. *Chem. Commun.* **2001**, *18*, 1740–1741. [CrossRef]
2. Chi, Y.; Chang, T.K.; Ganesan, P.; Rajakannu, P. Emissive bis-tridentate Ir(III) metal complexes: Tactics, photophysics and applications. *Coord. Chem. Rev.* **2017**, *346*, 91–100. [CrossRef]
3. Hong, Y.N.; Lam, J.W.Y.; Tang, B.Z. Aggregation-induced emission. *Chem. Soc. Rev.* **2011**, *40*, 5361–5388. [CrossRef] [PubMed]
4. Naithani, S.; Goswami, T.; Thetiot, F.; Kumar, S. Imidazo[4,5-f] [1,10] phenanthroline based luminescent probes for anion recognition: Recent achievements and challenges. *Coord. Chem. Rev.* **2023**, *475*, 214894. [CrossRef]
5. Pan, Z.Y.; Feng, W.W.; Liu, Q.Y.; He, L.; Yao, D.-H.; He, Z.-D. Lipophilic neutral iridium(III) complexes for phosphorescence imaging of lipid droplets and potential photodynamic therapy. *Dye. Pigm.* **2022**, *203*, 110387. [CrossRef]
6. Zhang, G.; Fu, X.; Zhou, D.; Hu, R.; Qin, A.; Tang, B.Z. Smart aggregation-induced emission polymers: Preparation, properties and bio-applications. *Smart Mol.* **2023**, *1*, 20220008. [CrossRef]
7. Manimaran, B.; Thanasekaran, P.; Rajendran, T.; Lin, R.J.; Chang, I.J.; Lee, G.H.; Peng, S.M.; Rajagopal, S.; Lu, K.L. Luminescence enhancement induced by aggregation of alkoxy-bridged rhenium(I) molecular rectangles. *Inorg. Chem.* **2002**, *41*, 5323–5325. [CrossRef]
8. Lin, S.H.; Pan, H.H.; Li, L.; Liao, R.; Yu, S.Z.; Zhao, Q.; Sun, H.B.; Huang, W. AIPE-active platinum(ii) complexes with tunable photophysical properties and their application in constructing thermosensitive probes used for intracellular temperature imaging. *J. Mater. Chem. C.* **2019**, *7*, 7893–7899. [CrossRef]
9. Sathish, V.; Ramdass, A.; Thanasekaran, P.; Lu, K.L.; Rajagopal, S. Aggregation-induced phosphorescence enhancement (AIPE) based on transition metal complexes-An overview. *J. Photochem. Photobiol. C.* **2015**, *23*, 25–44. [CrossRef]
10. Mauro, M.; Cebrián, C. Aggregation-induced phosphorescence enhancement in Ir(III) Complexes. *Isr. J. Chem.* **2018**, *58*, 901–914. [CrossRef]
11. Smith, A.R.G.; Burn, P.L.; Powell, B.J. Spin-orbit coupling in phosphorescent Ir(III) Complexes. *ChemPhysChem.* **2011**, *12*, 2428–2437. [CrossRef]
12. Jhun, B.H.; Song, D.; Park, S.Y.; You, Y. Phosphorescent Ir(III) complexes for biolabeling and biosensing. *Top. Curr. Chem.* **2022**, *380*, 35. [CrossRef] [PubMed]
13. Zhang, Q.; Chen, Y.; Liu, C. Living supramolecular polymerization of Ir(III) complexes. *Mol. Chem. Eng.* **2025**, *1*, 100008. [CrossRef]
14. Li, Y.Y.; Wu, Y.Q.; Wu, J.; Lun, W.C.; Zeng, H.; Fan, X.L. A near-infrared phosphorescent Ir(III) complex for fast and time-resolved detection of cysteine and homocysteine. *Analyst* **2020**, *145*, 2238–2244. [CrossRef] [PubMed]
15. Gao, H.F.; Qi, H.T.; Peng, Y.J.; Qi, H.L.; Zhang, C.X. Rapid "turn-on" photoluminescence detection of bisulfite in wines and living cells with a formyl bearing bis-cyclometalated Ir(III) complex. *Analyst* **2018**, *143*, 3670–3676. [CrossRef]
16. Yang, X.L.; Guo, H.R.; Liu, B.A.; Zhao, J.; Zhou, G.J.; Wu, Z.X.; Wong, W.Y. Diarylboron-based asymmetric red-emitting Ir(III) complex for solution-processed phosphorescent organic light-emitting diode with external quantum efficiency above 28%. *Adv. Sci.* **2018**, *5*, 1701067. [CrossRef]
17. Abbas, S.; Din, I.U.D.; Raheel, A.; Din, A.T.U. Cyclometalated Ir(III) complexes: Recent advances in phosphorescence bioimaging and sensing applications. *Appl. Organomet. Chem.* **2020**, *34*, 5413. [CrossRef]
18. Schreier, M.R.; Guo, X.W.; Pfund, B.; Okamoto, Y.; Ward, T.R.; Kerzig, C.; Wenger, O.S. Water-soluble tris(cyclometalated) Ir(III) complexes for aqueous electron and energy transfer photochemistry. *Acc. Chem. Res.* **2022**, *55*, 1290–1300. [CrossRef]
19. Zhao, Q.; Li, L.; Li, F.Y.; Yu, M.X.; Liu, Z.P.; Yi, T.; Huang, C.H. Aggregation-induced phosphorescent emission (AIPE) of iridium(III) complexes. *Chem. Commun.* **2008**, 685–687. [CrossRef]
20. Wei, R.H.; Chen, J.F.; Feng, J.Q.; Hu, J.S.; Cao, D.K. Two heteroleptic Ir(III)-bisthienylethene compounds: Syntheses, structures and aggregation-induced luminescence. *RSC Adv.* **2015**, *5*, 14359–14365. [CrossRef]
21. Dong, L.C.; Shang, G.J.; Shi, J.B.; Zhi, J.G.; Tong, B.; Dong, Y.P. Effect of substituent position on the photophysical properties of triphenylpyrrole isomers. *Phys. Chem. C.* **2017**, *121*, 11658–11664. [CrossRef]
22. Song, W.L.; Gao, J.; Gao, Y.; Shan, G.G.; Geng, Y.; Shao, K.Z.; Su, Z.M. Constructing anion-π interactions in cationic iridium (III) complexes to achieve aggregation-induced emission properties. *Inorg. Chem. Front.* **2024**, *11*, 1198–1206. [CrossRef]
23. Thekkathu, R.; Ashok, D.; Ramkollath, P.K.; Neelakandapillai, S.; Kurishunkal, L.P.; Yadav, M.S.P.; Kalarikkal, N. Magnetically recoverable Ir/IrO_2@Fe_3O_4 core/SiO_2 shell catalyst for the reduction of organic pollutants in water. *Chem. Phys. Lett.* **2020**, *742*, 137147. [CrossRef]
24. Paziresh, S.; Aghakhanpour, R.B.; Shahsavari, H.R.; Dolatyari, V.; Ara, I.; Nabavizadeh, S.M. Phosphorescent cyclometalated Ir(III) complexes comprising chelating thiolate ligands as pH-activatable sensors. *New J. Chem.* **2023**, *47*, 1378–1387. [CrossRef]
25. Lin, C.K.; Wang, J.; Yang, K.; Liu, J.B.; Ma, D.L.; Leung, C.H.; Wang, W.H. Development of a NIR iridium(III) complex for self-calibrated and luminogenic detection of boron trifluoride. *Spectrochim. Acta Part, A.* **2022**, *282*, 121658. [CrossRef]

26. Geng, T.M.; Ye, S.N.; Wang, Y.; Zhu, H.; Wang, X.; Liu, X. Conjugated microporous polymers-based fluorescein for fluorescence detection of 2,4,6-trinitrophenol. *Talanta* **2017**, *165*, 282–288. [CrossRef]
27. Tasci, E.; Aydin, M.; Gorur, M.; Gürek, A.G.; Yilmaz, F. Pyrene-functional star polymers as fluorescent probes for nitrophenolic compounds. *J. Appl. Polym. Sci.* **2018**, *135*, 46310. [CrossRef]
28. Fabin, M.; Lapkowski, M.; Jarosz, T. Methods for detecting picric acid-a review of recent progress. *Appl. Sci.* **2023**, *13*, 3991. [CrossRef]
29. Khan, I.; Shah, T.R.; Tariq, M.R.; Ahmad, M.; Zhang, B.L. Understanding the toxicity of trinitrophenol and promising decontamination strategies for its neutralization: Challenges and future perspectives. *J. Environ. Chem. Eng.* **2024**, *12*, 112720. [CrossRef]
30. Yi, S.L.; Lu, Z.; Xie, Z.H.; Hou, L.X. Amphiphilic gemini-iridium (III) complex for rapid and selective detection of picric acid in water and intracellular. *Talanta* **2020**, *208*, 120372. [CrossRef]
31. Shan, G.G.; Li, H.B.; Sun, H.Z.; Zhu, D.X.; Cao, H.T.; Su, Z.M. Controllable synthesis of iridium(III)-based aggregation-induced emission and/or piezochromic luminescence phosphors by simply adjusting the substitution on ancillary ligands. *J. Mater. Chem. C* **2013**, *1*, 1440–1449. [CrossRef]
32. Yang, C.; Wen, L.L.; Shan, G.G.; Sun, H.Z.; Mao, H.T.; Zhang, M.; Su, Z.M. Di-/trinuclear cationic Ir(III) complexes: Design, synthesis and application for highly sensitive and selective detection of TNP in aqueous solution. *Sens. Actuators B.* **2017**, *244*, 314–322.
33. Chen, R.M.; Zhang, Q.L.; Zhang, L.Y.; Liu, C. A phenyl-modified aggregation-induced phosphorescent emission-active cationic Ru(II) complex for detecting picric acid in aqueous media. *Chemosensors* **2025**, *13*, 14. [CrossRef]
34. Xu, J.C.; Zhang, L.Y.; Shi, Y.S.; Liu, C. Carbazolyl-modified neutral Ir(III) complexes for efficient detection of picric acid in aqueous media. *Sensors* **2024**, *24*, 4074. [CrossRef]
35. Yan, Y.Y.; Jia, W.H.; Zhang, L.Y.; Liu, C. Fluorophenyl-modified AIPE-active cationic Pt(II) complexes for detecting picric acid in aqueous media. *Dye. Pigm.* **2023**, *220*, 111719. [CrossRef]
36. Liu, C.; Rao, X.F.; Song, X.L.; Qiu, J.S.; Jin, Z.L. Palladium-catalyzed ligand-free and aqueous Suzuki reaction for the construction of (hetero)aryl-substituted triphenylamine derivatives. *RSC Adv.* **2013**, *3*, 526–531. [CrossRef]
37. Wang, R.J.; Deng, L.J.; Zhang, T.; Li, J.Y. Substituent effect on the photophysical properties, electrochemical properties and electroluminescence performance of orange-emitting iridium complexes. *Dalton Trans.* **2012**, *41*, 6833–6841. [CrossRef] [PubMed]
38. Toprak, M.; Aydin, B.M.; Arik, M.; Onganer, Y. Fluorescence quenching of fluorescein by Merocyanine 540 in liposomes. *J. Lumin.* **2011**, *131*, 2286–2289. [CrossRef]
39. Xiang, Q.; Qiu, Q.X.; Zhang, C.; Zhang, J.F. Unique cluster-metal framework constructed by multidentate N-donating ligand for TNP detection. *J. Clust. Sci.* **2022**, *33*, 1149–1156. [CrossRef]
40. Han, Y.Y.; Zhao, J.X.; Yang, H.C.; Huang, X.T.; Zhou, X.Y.; Hui, T.Q.; Yan, J. Synthesis of new fluorene compounds for highly selective sensing of picric acid, Fe^{3+} and L-arginine. *J. Mol. Struct.* **2020**, *1217*, 128395. [CrossRef]
41. Zhang, L.; Hu, J.S.; Li, J.X.; Zhang, J. A thermal and pH stable fluorescent coordination polymer for sensing nitro explosives or metal ions with high selectivity and sensitivity in aqueous solution. *J. Lumin.* **2021**, *234*, 117958. [CrossRef]
42. Wang, J.; Wang, D.; Miller, E.K.; Moses, D.; Heeger, A.J. Static and dynamic photoluminescence (PL) quenching of polymer: Quencher systems in solutions. *Synth. Met.* **2001**, *119*, 591–592. [CrossRef]
43. Ciotta, E.; Prosposito, P.; Pizzoferrato, R. Positive curvature in Stern-Volmer plot described by a generalized model for static quenching. *J. Lumin.* **2019**, *206*, 518–522. [CrossRef]
44. Zu, F.L.; Yan, F.Y.; Bai, Z.J.; Xu, J.X.; Wang, Y.Y.; Huang, Y.C.; Zhou, X.G. The quenching of the fluorescence of carbon dots: A review on mechanisms and applications. *Microchim. Acta.* **2017**, *184*, 1899–1914. [CrossRef]
45. Gadomska, A.V.; Nevidimov, A.V.; Tovstun, S.A.; Petrova, O.V.; Sobenina, L.N.; Trofimov, B.A.; Razumov, V.F. Fluorescence from 3,5-diphenyl-8-CF_3-BODIPYs with amino substituents on the phenyl rings: Quenching by aromatic molecules. *Spectrochim. Acta Part A.* **2021**, *254*, 119623. [CrossRef] [PubMed]
46. Hollett, G.; Roberts, D.S.; Sewell, M.; Wensley, E.; Wagner, J.; Murray, W.; Krotz, A.; Toth, B.; Vijayakumar, V.; Sailor, M.J. Quantum ensembles of silicon nanoparticles: Discrimination of static and dynamic photoluminescence quenching processes. *J. Phys. Chem. C.* **2019**, *123*, 17976–17986. [CrossRef]
47. Shyamal, M.; Maity, S.; Mazumdar, P.; Sahoo, G.P.; Maity, R.; Misra, A. Synthesis of an efficient Pyrene based AIE active functional material for selective sensing of 2,4,6-trinitrophenol. *J. Photochem. Photobiol. A* **2017**, *342*, 1–14. [CrossRef]

Disclaimer/Publisher's Note: The statements, opinions and data contained in all publications are solely those of the individual author(s) and contributor(s) and not of MDPI and/or the editor(s). MDPI and/or the editor(s) disclaim responsibility for any injury to people or property resulting from any ideas, methods, instructions or products referred to in the content.